Estimating the time of pockmark formation in the SW Xisha Uplift (South China Sea) using reaction-transport modeling

Min Luo [a,e], Andrew W. Dale [b], Klaus Wallmann [b], Christian Hensen [b], Joris Gieskes [d], Wen Yan [c], Duofu Chen [a,c,*]

[a] Key Laboratory of Marginal Sea Geology, Guangzhou Institute of Geochemistry, Chinese Academy of Sciences, Guangzhou 510640, China
[b] GEOMAR Helmholtz Centre for Ocean Research, Kiel 24148, Germany
[c] Key Laboratory of Marginal Sea Geology, South China Sea Institute of Oceanology, Chinese Academy of Sciences, Guangzhou 510301, China
[d] Scripps Institution of Oceanography, La Jolla, San Diego, CA, USA
[e] University of Chinese Academy of Sciences, Beijing 100049, China

ABSTRACT

Carbon cycling and fluid seepage in marine sediments over the late Quaternary were investigated at a now-extinct pockmark located in a mega-pockmark field in the SW Xisha Uplift (NW South China Sea). Measured particulate organic carbon (POC) content, and porewater sulfate (SO_4^{2-}), dissolved inorganic carbon (DIC) concentrations and $\delta^{34}S$-SO_4^{2-} distributions were used to constrain a non-steady-state reaction-transport model and quantify POC mineralization rates as well as estimate the time when fluid flow ceased at the investigated pockmark. An increase in POC content and $\delta^{34}S$-SO_4^{2-} and a decrease in sulfate concentrations in the upper ca. 2 m at the pockmark and a reference core implied an increase in the flux and reactivity of organic matter during the early Holocene around 10 kyr B. P. caused by enhanced primary productivity during the strengthened southwestern summer monsoon. These features were simulated with the model assuming a Holocene increase in POC flux and reactivity. Subsequently, starting from an initial condition reminiscent of a modern active cold seep (Hydrate Ridge), hindcast simulations showed that fluid seepage at the pockmark ceased ca. 39 kyr ago. This corresponds to a relative sea level high-stand, which is believed to be associated with gas hydrate stabilization. The non-steady-state model presented in this contribution can also be used to constrain the time when fluid seepage ceased at other presently extinct cold seeps when suitable sediment and porewater data are available.

© 2015 Elsevier B.V. All rights reserved.

1. Introduction

Migration of sediment pore fluid in the seafloor is characteristic of both passive and active continental margins (Judd and Hovland, 2007). The latter are characterized by tectonically driven sediment compaction, faulting and fracturing of the overburden and resulting vertical fluid advection. Advection rates here are assumed to be much greater compared to non-tectonic passive margins (Minshull and White, 1989; Suess et al., 1999; Archer and Buffett, 2012). Despite a lack of continuous tectonic compression, conspicuous features of focused fluid flow have been observed on modern passive margins such as mud volcanoes, pockmarks, hydrate mounds and carbonate slabs (Bouriak et al., 2000; Hustoft et al., 2009a; Wang et al., 2010; Sun et al., 2012b, 2013). Slow upward migration of these fluids, typically enriched in hydrocarbons, creates so called 'cold seeps', which are often regarded as windows to the deep biogeosphere. Cold seeps have guided the exploration of hydrocarbons and support abundant chemosynthetic macrofauna and microbial communities (Heggland, 1998;

Hovland and Svensen, 2006; Foucher et al., 2009). In addition, the release of methane from sediments to the water column and, possibly, the atmosphere is of environmental importance because methane is a potent greenhouse gas (Judd et al., 2002; MacDonald et al., 2002). Furthermore, fluid release is also associated with seabed instability (Hovland et al., 2002; Berndt, 2005). Better quantification of fluid flow is thus needed to better quantify carbon emissions from the seafloor.

Pockmarks are among the most common manifestations of fluid flow on the seafloor and are widespread along continental margins (Çifçi et al., 2003; Hovland et al., 2005; Pilcher and Argent, 2007; León et al., 2010). They are seabed depressions of various sizes and morphologies that are generally created either by catastrophic eruption of methane gas or by slow and continuous fluid seepage (Hovland et al., 2002). Discoveries of pockmarks in the northern South China Sea (SCS) have been ongoing as part of exploration of hydrocarbons and gas hydrate reserves (Chow et al., 2000; Wang et al., 2010). Recently, mega-pockmarks (>1000 m in diameter) were documented in the SW Xisha Uplift (NW SCS) and they may have been caused by active fluid flow as well as strong bottom currents (Sun et al., 2011). Geochemical analysis of sediment porewater suggested that the pockmarks are presently inactive and possibly in a quiescent period (Luo et al., 2013). The timing of fluid flow and the widespread development of pockmarks in this area

remain poorly constrained. Nonetheless, this information is important to understand past fluid flow and its formation trigger mechanisms. The temporal history of paleo-seepage features such as pockmarks could further provide evidence for a possible link between methane release from the seafloor and carbon isotopic excursions in the paleo-climatic record (Dickens et al., 1997; Zachos et al., 2008). Seismic interpretation has been successfully utilized to infer the timing and mechanism of paleo-pockmark formation (Cole et al., 2000; Hustoft et al., 2009b; Andresen and Huuse, 2011; Hartwig et al., 2012; Moss et al., 2012). Isotopic dating of organic carbon, planktonic foraminifera, cold seep fauna, and authigenic carbonates has also been used to elucidate the time of pockmark formation and the historical evolution of fluid seepage (Paull et al., 2002, 2008; Feng et al., 2010; Hill et al., 2012; Taviani et al., 2013).

Our present objective is to understand the timing of pockmark formation in the NW SCS using non-steady-state model approaches (e.g., Mogollón et al., 2012). Hindcast model simulations of a hypothetical fluid seep constrained by geochemical measurements are used to predict the minimum age of the formation of a now-extinct or dormant pockmark in the SW Xisha Uplift. The rates of organic matter degradation and associated biogeochemical processes in pockmarks are also described. The juxtaposition of seepage termination and sea level high-stand leads us to suggest that pockmark activity may be related to variations in the size of the gas hydrate reservoir due to sea level fluctuations.

2. Study area

The northern SCS margin is a passive continental setting bounded to the west by a transform zone toward Indochina and to the east by a sub-duction zone toward the Philippine arc (Clift et al., 2002; Lüdmann et al., 2005). The study area is located in the SW Xisha Uplift (Fig. 1) with the
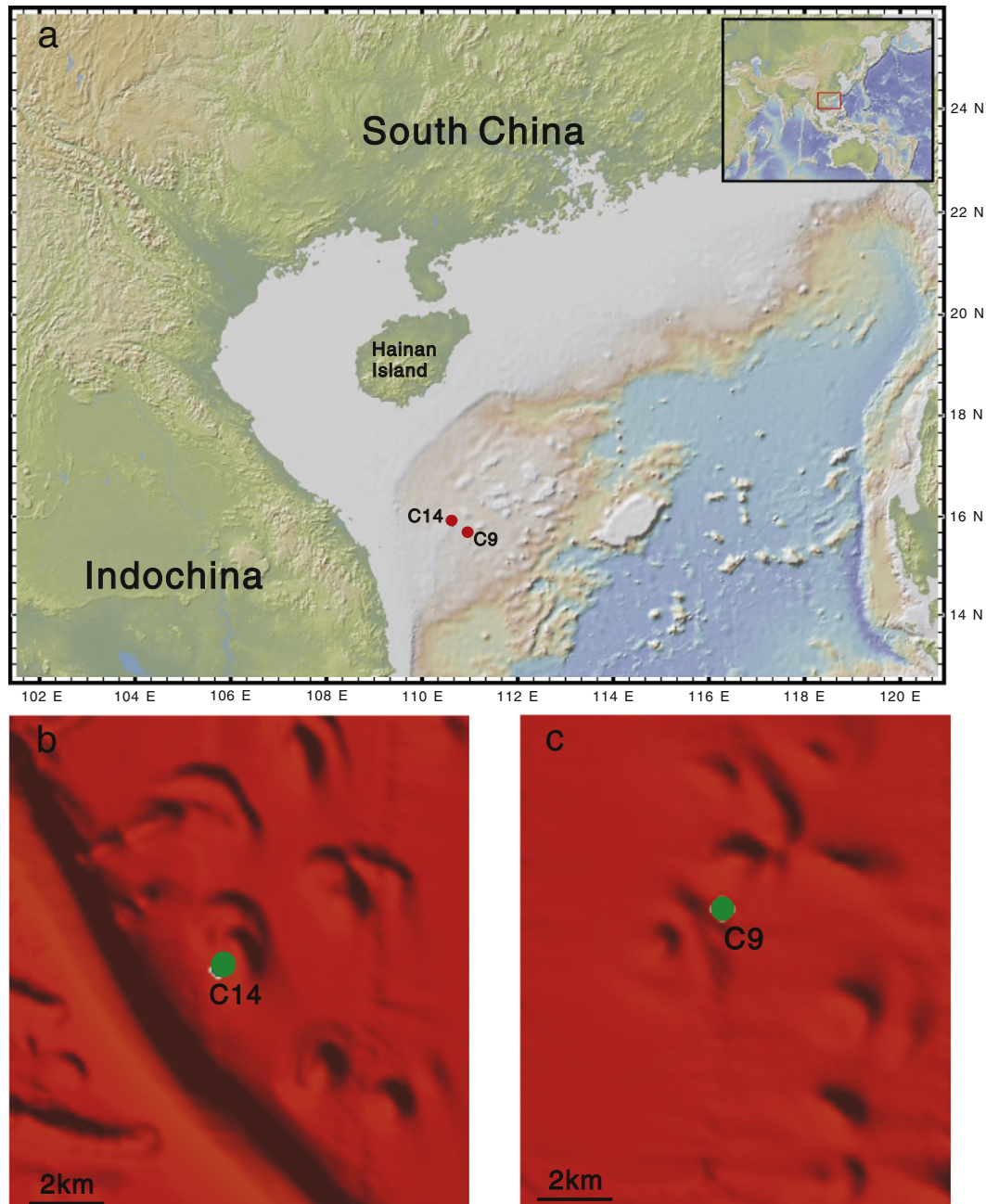

Fig. 1. (a) Map of the study area and sampling sites. The multibeam bathymetric maps in (b) and (c) show the location of the cores relative to the pockmarks.

sedimentary filling similar to that of the Cenozoic rift basins in the northern SCS. The structural evolution can be divided into Eocene–Oligocene rift and Neocene–Quaternary post-rift subsidence (Robison et al., 1998; Xie et al., 2006). The sedimentary layers deposited during the Eocene–Oligocene rift are characterized by lacustrine and neritic mudstone facies and coastal plain coal-bearing layers, which are the primary high-quality source rock for hydrocarbon generation. The sedimentary layers of Neocene–Quaternary post-rift subsidence are mainly composed of neritic shelf sandstones and neritic–hemipelagic–pelagic calcareous mudstones, which are effective reservoirs and seals for hydrocarbon fluid (Huang et al., 2003; Zhu et al., 2009).

The majority of the pockmarks in the study area are classed as mega-pockmarks (1000–2500 m in diameter and 60–140 m in depth) with an areal density of ca. 0.4–1 km^{-2}. Their distribution is associated with underlying fluid migration structures, such as gas chimneys, faults, unconformities, polygonal faults and paleo-channels (Sun et al., 2011). Due to rapid sediment loading and the resulting under-compaction, overpressure accumulated throughout much of the study area during the Cenozoic. In conjunction with high temperature-induced maturity of source rock (geothermal gradient, 39–41 °C km^{-1}), this led to upward migration of hydrocarbons toward the seabed and pockmark formation (Sun et al., 2012a). In addition, distinct bottom simulating reflectors (BSRs) indicative for the phase boundary between free gas and solid gas hydrate have been described for this area (Wang et al., 2010). Furthermore, compelling evidence for the gas hydrate dissociation such as chlorinity decrease in tandem with porewater $\delta^{18}O$ increase has been observed at core C14 in the pockmark field (Luo et al., 2014).

3. Sampling and methods

3.1. Sampling

The porewater concentrations shown here have been published previously (Luo et al., 2013), whereas particulate organic matter (POC) content is new to this study. Two sediment cores were retrieved using gravity–piston corers from the SW Xisha Uplift during the Shiyan-1 cruise led by the South China Sea Institute of Oceanology, Chinese Academy of Sciences (CAS) in May 2012. Core C9 (15°41.032′N, 110°57.246′E; water depth, 829 mbsl (meters below sea level); core length, 7.6 m) was sampled from outside a mega-pockmark and taken as the reference core. Core C14 (15°54.507′N, 110°38.607′E; water depth, 840 mbsl; core length, 6.7 m) was collected from inside a mega-pockmark and is termed the pockmark core (Fig. 1). Surface sediments were lost during gravity–piston coring. However, given the similarity of sulfate and DIC concentrations in the uppermost sample and typical bottom water values, we estimate that the lost interval is probably only a few centimeters at most. Porewater was sampled in the onboard laboratory by means of Rhizon samplers consisting of a porous polymer tube with integrated filter (20 μm). Aliquots of porewater were extracted using a syringe under vacuum, preserved with 10 μl saturated HgCl$_2$ solution and stored at 4 °C under a N$_2$ headspace.

3.2. Analytical methods

Porewater samples were diluted 1:500 and 1:200 with ultrapure water to determine the concentrations of SO_4^{2-} and Ca^{2+}, respectively, using a Dionex ICS-900 ion chromatograph. An Ion Pac AS23-type column and a 4.5 mM Na$_2$CO$_3$ + 0.8 mM NaHCO$_3$ mixed solution in an anion system were used to determine sulfate concentration. An Ion Pac CS12A-type column and an 11 mM H$_2$SO$_4$ solution in a cation system were used to determine Ca^{2+} concentration. The analytical precision for all ions was ±2% as determined by measurement of IAPSO standard water. DIC concentration was determined using an IsoPrime 100 continuous flow isotope ratio mass spectrometer (CF-IRMS) after acidifying the sample with pure H$_3$PO$_4$. NaHCO$_3$ samples with concentrations of 0.85 mM, 2.07 mM, and 3.93 mM were used as standards.

The analytical precision of the DIC concentration was <2%. For the measurement of particulate organic carbon (POC) content, 100 mg of sediment powder was first digested in 2–3 ml 10% HCl for 12 h to remove carbonates. The residues were analyzed for carbon content using a Vario EI-III elemental analyzer with an analytical error better than 0.03%. All the above measurements were performed at the State Key Laboratory of Isotope Geochemistry, Guangzhou Institute of Geochemistry, CAS.

For the sulfur isotope measurements, dissolved sulfate was precipitated as barium sulfate by the addition of an excess of barium chloride within 1 h after acidification. Samples of barium sulfate were converted to SO$_2$ by combustion with Cu$_2$O in a high vacuum extraction line, and the SO$_2$ was then analyzed with a delta-S mass spectrometer in the Laboratory for Stable Isotope Geochemistry, Institute of Geology and Geophysics, CAS. Replicate measurements of the international standard IAEAS2 agreed within ± 0.3‰. The results were expressed as per mil difference relative to the V-CDT (Vienna-Canyon Diablo Troilite) standard.

4. Numerical modeling

A reaction-transport model was used to simulate one solid species (POC) and five dissolved species including sulfate (SO_4^{2-}), methane (CH$_4$), dissolved inorganic carbon (DIC), calcium (Ca^{2+}) and ^{34}S-SO_4^{2-} (hereafter $^{34}SO_4^{2-}$). The latter was used to simulate the stable isotopic composition of sulfate, δ^{34}S-SO_4^{2-} (‰). The model solves the following partial differential equations for solutes (Eq. (1)) and POC (Eq. (2)) (Berner, 1980; Wallmann et al., 2006a):

$$\Phi \frac{\partial C_a}{\partial t} = \frac{\partial \left(\Phi \cdot D_s \cdot \frac{\partial C_a}{\partial x} \right)}{\partial x} - \frac{\partial \left(\Phi \cdot v_p \cdot C_a \right)}{\partial x} + \Phi \cdot \Sigma R \tag{1}$$

$$(1-\Phi) \frac{\partial POC}{\partial t} = -\frac{\partial ((1-\Phi) \cdot v_s \cdot POC)}{\partial x} + (1-\Phi) \cdot \Sigma R \tag{2}$$

where x (cm) is depth, t (yr) is time, Φ is porosity, D_s (cm^2 yr^{-1}) is the molecular diffusion coefficient corrected for tortuosity, C_a (μmol cm^{-3}) is the concentration of dissolved species, POC is in wt.%, v_p (cm yr^{-1}) is the burial velocity of porewater, v_s (cm yr^{-1}) is the burial velocity of solids and ΣR denotes the sum of the rates of biogeochemical reactions considered in the model. Measured data used to constrain the model were obtained from the upper ca. 7 m of sediments. The major processes considered in the model that are relevant to these length scales in this setting include organic matter degradation via sulfate reduction and methanogenesis, anaerobic oxidation of methane (AOM), and authigenic carbonate precipitation. Organic matter mineralization by aerobic respiration, denitrification, manganese reduction, and iron reduction were ignored since these are typically confined to the upper 10–20 cm (Van Cappellen and Wang, 1996). For similar reasons, bioturbation and bioirrigation were not considered. Besides, this layer was probably not fully captured by the gravity–piston corer. Fixed model parameters are listed in Table 1.

Sediment porosity decreases with depth assuming steady-state compaction:

$$\Phi = \Phi_f + \left(\Phi_0 - \Phi_f \right) \cdot e^{-px} \tag{3}$$

where Φ_f and Φ_0 are the porosity below the depth of compaction and at sediment surface, and p (cm^{-1}) is the depth attenuation coefficient for porosity (Wang et al., 2000).

In the absence of externally-imposed fluid advection at the present seafloor, the velocity of porewater and solids is directed downward under steady-state compaction relative to the seafloor:

$$v_p = \frac{\Phi_f \cdot \omega}{\Phi} \tag{4}$$

Table 1

Summary of model parameters and boundary conditions for the reference core (C9) and pockmark core (C14).

Parameter	C9	C14	Unit
Temperature (T)	5	4.9	°C
Salinity (S)	33.5	34	–
Pressure (P)	8.4	8.5	MPa
Density of dry solids (ρ_s)	2.5	2.5	g cm^{-3}
Sedimentation rate (ω) [a]	0.033	0.033	cm yr^{-1}
Porosity at sediment–water interface (Φ_0) [b]	0.7	0.7	–
Porosity in compacted sediments (Φ_f) [b]	0.54	0.54	–
Depth attenuation coefficient for porosity (p) [b]	0.005	0.005	–
Molecular diffusion coefficient of SO$_4^{2-}$ in free seawater	191	191	cm^2 yr^{-1}
Molecular diffusion coefficient of ^{34}SO$_4^{2-}$ in free seawater	191	191	cm^2 yr^{-1}
Molecular diffusion coefficient of CH$_4$ in free seawater	294	294	cm^2 yr^{-1}
Molecular diffusion coefficient of DIC in free seawater [c]	203	203	cm^2 yr^{-1}
Molecular diffusion coefficient of Ca^{2+} in free seawater	142	142	cm^2 yr^{-1}
POC inhibition constant (K_c) [d]	35	35	mM
Michaelis–Menten constant for POC degradation $(K_{SO_4^{2-}})$ [d]	0.1	0.1	mM
Kinetic constant for AOM (k_{AOM}) [d]	1	1	cm^3 yr^{-1} mmol^{-1}
Upper boundary condition for SO$_4^{2-}$	28.2	28.9	mM
Upper boundary condition for ^{34}SO$_4^{2-}$	0.129	0.132	mM
Upper boundary condition for DIC	2.7	2.4	mM
Upper boundary condition for CH$_4$	0	0	mM
Upper boundary condition for Ca^{2+}	10.3	9.9	mM
Lower boundary condition for SO$_4^{2-}$	$\partial C/\partial x = 0$	$\partial C/\partial x = 0$	–
Lower boundary condition for ^{34}SO$_4^{2-}$	$\partial C/\partial x = 0$	$\partial C/\partial x = 0$	–
Lower boundary condition for DIC	$\partial C/\partial x = 0$	$\partial C/\partial x = 0$	–
Lower boundary condition for CH$_4$	$\partial C/\partial x = 0$	$\partial C/\partial x = 0$	–
Lower boundary condition for Ca^{2+}	$\partial C/\partial x = 0$	$\partial C/\partial x = 0$	–

[a] Mean value derived from the six ODP184 drillings in SCS (Wang et al., 2000).
[b] Modified after Wang et al. (2000).
[c] Based on the molecular diffusion coefficient of bicarbonate ion.
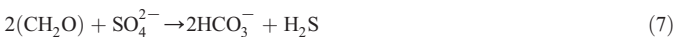[d] Wallmann et al. (2006a).

Table 2

Net rate expressions of all species applied in the model.

Species	Rates
Particulate organic carbon (POC)	$-R_{POC}$
Sulfate (SO$_4^{2-}$)	$-R_{SR}-R_{AOM}$
Heavy sulfur isotope of sulfate (^{34}SO$_4^{2-}$)	$-R_{hSR}$
Calcium (Ca^{2+})	$-R_{PPT}$
Dissolved inorganic carbon (DIC)	$R_{DP} + R_{AOM}-R_{PPT}$
Methane (CH$_4$)	$R_{MG}-R_{AOM}$

organic matter is degraded fermentatively by methanogens to produce methane and carbon dioxide:

$$2(CH_2O) \rightarrow CO_2 + CH_4. \tag{8}$$

The rates of sulfate reduction and methanogenesis depend on the total rate of POC degradation, R_{POC} (g C g^{-1} yr^{-1}), according to Middelburg (1989) and later modified by Wallmann et al. (2006a):

$$R_{POC} = \frac{K_C}{[DIC] + [CH_4] + K_C} \cdot \left(0.16 \cdot \left(a_0 + \frac{x}{v_s} \right)^{-0.95} \right) \cdot POC \tag{9}$$

where K_c is an inhibition constant for POC degradation due to DIC and CH$_4$ accumulation in the porewater. [DIC] and [CH$_4$] are the simulated concentrations of DIC and CH$_4$ respectively, and a_0 is the initial age of organic matter reflecting the reactivity of organic matter that arrives at the seafloor (Middelburg, 1989). The rates of sulfate consumption via organoclastic sulfate reduction (OSR) (R_{SR}, μmol cm^{-3} yr^{-1} of SO$_4^{2-}$), methane production by methanogenesis (R_{MG}, μmol cm^{-3} yr^{-1} of CH$_4$), and DIC production via POC decomposition (R_{DP}, μmol cm^{-3} yr^{-1} of carbon) are thus dependent on R_{POC}:

$$R_{SR} = 0.5 \cdot \frac{\rho_s \cdot (1-\Phi) \cdot 10^6}{MW_C \cdot \Phi} \cdot \frac{\left[SO_4^{2-} \right]}{\left[SO_4^{2-} \right] + K_{SO_4^{2-}}} \cdot R_{POC} \tag{10}$$

$$R_{MG} = 0.5 \cdot \frac{\rho_s \cdot (1-\Phi) \cdot 10^6}{MW_C \cdot \Phi} \cdot \frac{K_{SO_4^{2-}}}{\left[SO_4^{2-} \right] + K_{SO_4^{2-}}} \cdot R_{POC} \tag{11}$$

$$R_{DP} = \frac{\rho_s \cdot (1-\Phi) \cdot 10^6}{MW_C \cdot \Phi} \cdot R_{POC} - R_{MG} \tag{12}$$

where ρ_s is the density of dry sediments, MW_C is the atomic weight of carbon, and $K_{SO_4^{2-}}$ is the Michaelis–Menten constant for the inhibition of sulfate reduction at low sulfate concentrations.

The anaerobic oxidation of methane (AOM) coupled sulfate reduction mediated by a syntrophic consortium of methanotrophic archaea and sulfate-reducing bacteria, is an important sink for sulfate in anoxic marine sediments (Reeburgh, 1976; Boetius et al., 2000):

$$CH_4 + SO_4^{2-} \rightarrow HCO_3^- + HS^- + H_2O. \tag{13}$$
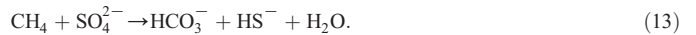
The rate of AOM (R_{AOM}) was calculated using bimolecular kinetics e.g., Regnier et al. (2011):

$$R_{AOM} = k_{AOM} \cdot \left[SO_4^{2-} \right] \cdot [CH_4] \tag{14}$$

where k_{AOM} is the rate constant.

The rate of Ca^{2+} and DIC precipitation into authigenic carbonates was estimated from the concentration difference between modeled and measured Ca^{2+} concentrations (R_{PPT}):

$$R_{PPT} = k_{PPT} \cdot \left(\left[Ca^{2+} \right] - \left[Ca^{2+} \right]_T \right) \tag{15}$$

$$v_s = \frac{\left(1-\Phi_f \right) \cdot \omega}{(1-\Phi)} \tag{5}$$

where ω (cm yr^{-1}) is the sedimentation rate derived from six cores in the SCS (Wang et al., 2000). Depth-dependent molecular diffusion coefficients of dissolved species were calculated after Boudreau (1997) and Oelkers and Helgeson (1991) and corrected for the effect of tortuosity:

$$D_s = \frac{D_m}{1-ln(\Phi)^2} \tag{6}$$

where D_m is the molecular diffusion coefficient in free seawater at the in situ temperature, salinity and pressure.

The net reaction terms of all species used in the model are summarized in Table 2. The mineralization of organic matter provides the principal energy source for microbial activity in marine sediments (Froelich et al., 1979). Below the surface oxidized layer, dissolved sulfate is the main electron acceptor used by microbes in anaerobic marine sediments (Jørgensen and Kasten, 2006). The mineralization of organic matter via sulfate reduction can be represented in simplified form:

$$2(CH_2O) + SO_4^{2-} \rightarrow 2HCO_3^- + H_2S \tag{7}$$

where CH$_2$O is the nominal stoichiometry of POC with a zero oxidation state. When sulfate is almost completely consumed, the remaining

where k_{PPT} is the first-order rate constant and $[Ca^{2+}]_T$ represents the observed Ca^{2+} concentration which is almost constant below ca. 1.5 mbsf (meters below seafloor) at 6 mM for C9 and 5.8 mM for C14.

Since sulfate-reducing bacteria typically discriminate against ^{34}S and preferentially consume ^{32}S during bacterial sulfate reduction, the residual sulfate will become progressively enriched in the heavy isotope (Habicht and Canfield, 1997). The $\delta^{34}S$-SO_4^{2-} was simulated by considering $^{34}SO_4^{2-}$ as a separate species (Jørgensen, 1979; Chernyavsky and Wortmann, 2007; Dale et al., 2009; Wortmann and Chernyavsky, 2011):

$$\phi SO_4^{2-} = \frac{\left[^{34}SO_4^{2-}\right]}{\left[SO_4^{2-}\right]} \qquad (16)$$

$$R_{hSR} = \frac{\phi SO_4^{2-}}{\phi SO_4^{2-} + \alpha_{SR} - \alpha_{SR} \cdot \phi SO_4^{2-}} \cdot (R_{SR} + R_{AOM}) \qquad (17)$$

$$\delta^{34}S = \frac{\left(^{34}S/^{32}S\right)_{VCDT} - \phi SO_4^{2-} - \left(^{34}S/^{32}S\right)_{VCDT} \cdot \phi SO_4^{2-}}{\left(^{34}S/^{32}S\right)_{VCDT} \cdot \left(\phi SO_4^{2-} - 1\right)} \cdot 1000 \qquad (18)$$

where ΦSO_4^{2-} is mole fraction of $^{34}SO_4^{2-}$, $[^{34}SO_4^{2-}]$ is the modeled concentration of $^{34}SO_4^{2-}$, R_{hSR} is the rate of $^{34}SO_4^{2-}$ consumption by OSR and AOM, α_{SR} is the fractionation factor for the reduction of sulfate to H_2S and $(^{34}S/^{32}S)_{VCDT}$ is the standard sulfur isotopic ratio in Vienna Canyon Diablo Troilite (0.00450045). α_{SR} is a tuning parameter constrained by the measured $\delta^{34}S$-SO_4^{2-} data.

To solve the model, the upper boundaries for solutes were set to measured values at the top of the core (Dirichlet-type boundary), assuming a CH_4 concentration of zero. The upper boundary for POC was prescribed as a flux (Robin-type boundary). A zero concentration gradient (Neumann-type boundary) was imposed at the lower boundary condition for all species. The length of the sediment column was set large enough (100 m) to ensure near-completeness of methanogenesis within the model domain. The continuous differential equations in Eqs. (1) and (2) were discretized using finite difference and the method-of-lines over an uneven grid (2000 layers) with a high resolution at the surface (0.05 cm) and lower resolution toward the bottom (19 cm). The model was solved using the NDSolve object of MATHEMATICA V. 8.0. As explained in the following section, the model was run in a non-steady-state configuration whereby the POC flux to the seafloor was varied over time.

5. Results and discussion

5.1. Organic matter mineralization in the reference core

POC content in the reference core (C9) decreased from ca. 0.9% at the surface to ca. 0.6% at ca. 1.5 mbsf. Below this depth, POC showed little variability, suggesting the accumulation and burial of poorly reactive material. The sulfate concentration also decreased from ca. 28 mM to ca. 21 mM at 7 mbsf, with a marked change in the concentration gradient centered at ca. 1–2 mbsf (Fig. 2). This coincides with the decrease in POC content and increase in $\delta^{34}S$-SO_4^{2-} from bottom water value (ca. 20‰) to ca. 26‰. Below ca. 2 mbsf, sulfate decreased linearly down to
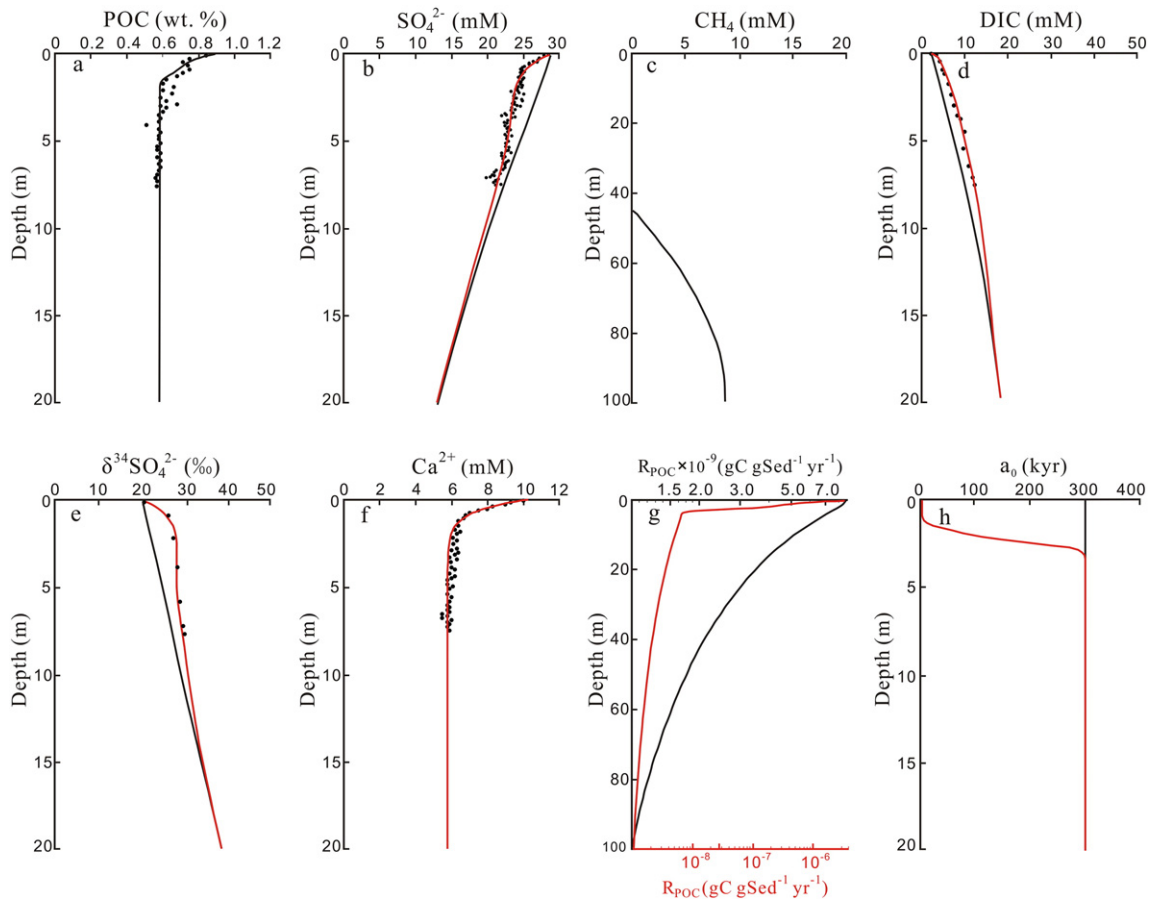
Fig. 2. Non-steady-state model results for the reference core C9 include (a) POC, (b) sulfate, (c) methane, (d) DIC, (e) $\delta^{34}S$-SO_4^{2-}, (f) calcium, (e) R_{POC} and (h) initial age of POC. Symbols represent measured data. Black lines are the model profiles where the POC flux was increased from 2.4×10^{-4} to 3.6×10^{-4} g cm^{-2} yr^{-1} over the last 10 kyr. Red lines are the results with the same increase in POC flux in addition to a decrease in the initial age from 300 to 0.5 kyr. The profiles of POC and methane in the two scenarios are almost identical and only the black lines are shown. Authigenic carbonate precipitation is only incorporated in the model of Scenario #2 during the last 10 kyr (f). Note the different depth scales.

Table 3

Summary of model-derived parameters for the reference core (C9) and pockmark core (C14).

Parameter	C9	C14	Unit
Flux of POC at sediment surface for $t \leq 10$ kyr	2.4×10^{-4}	2×10^{-4}	$g\ cm^{-2}\ yr^{-1}$
Flux of POC at sediment surface for $t > 10$ kyr	3.6×10^{-4}	3.2×10^{-4}	$g\ cm^{-2}\ yr^{-1}$
Initial age (a_0) for $t \leq 10$ kyr	300	300	kyr
Initial age (a_0') for $t > 10$ kyr	0.5	0.5	kyr
Kinetic constant of authigenic carbonate precipitation/dissolution (k_{PPT})	0.02	0.03	yr^{-1}
Sulfate fractionation factor during sulfate reduction (α_{SR})	1.045	1.051	–

the bottom of the sampled core, indicative of a sink at greater depth. The lowest $\delta^{13}C$-DIC value is only -12.5‰ which could be a mixture of POC-derived DIC and bottom water DIC (Luo et al., 2013). These observations together suggest that OSR is the major sink for sulfate in the upper 2 m, whereas AOM appears to play a role in sulfate consumption in the deep-seated sediments that are beyond the reach of the piston corer (Borowski et al., 1999). The DIC produced by these pathways is partly precipitated as authigenic carbonates, as indicated by the decrease in calcium concentrations in upper ca. 1.5 m sediments. However, even though these processes as well as methanogenesis below the AOM zone probably dominate the carbon cycle in the sediments sampled here, steady-state simulations of organic matter degradation model fail to capture the simultaneous decrease in POC and sulfate as well as the accumulation of DIC and $^{34}SO_4$ (model results not shown). In fact, similar kink-type sulfate profiles have been attributed to non-steady-state diagenesis (Hensen et al., 2003). Based on the regional sedimentation rate (Wang et al., 2000) and the depth of the kinks in the profiles of POC content, sulfate concentration and $\delta^{34}S$-SO_4^{2-} values (1–2 mbsf), there may have been an increase in the flux and/or reactivity of organic matter to the seafloor within the last several kyr over this layer.

There is evidence for an increase in the delivery of organic matter to the sediments in the SCS during the early Holocene driven by enhanced primary productivity. Primary production in the SCS is mainly controlled by the prevailing monsoon and terrigenous nutrient inputs (Tian et al., 2004). Previous studies showed that the surface organic carbon content is extraordinarily high along the southeastern Sunda Shelf, the northeastern slope of the SCS and offshore eastern Vietnam (Chen et al., 2010). Our study area is located off the east coast of Vietnam, where intensified summer monsoons during the Holocene have resulted in upwelling and enhanced primary productivity (Liu et al.,

2002). Abundances of *Florisphaera profunda* in sediment cores, one of the lower euphotic zone species of coccolithophores, as well as a rise in sediment Ba/Al and Br/Al suggested that primary productivity and organic matter rain rates to the seafloor have been increasing since the early Holocene in the NW SCS (Su et al., 2007; He et al., 2012). Thus, we hypothesize that enhanced primary productivity induced by the strengthened southwestern summer monsoon is responsible for the observed features in the POC, sulfate, and $\delta^{34}S$-SO_4^{2-} data in the upper 1–2 m of sediments.

Based on these observations, we performed non-steady-state model simulation with the aim of testing this hypothesis. We began by determining the POC flux and initial age of POC in the pre-Holocene setting, that is, based on the data below 2 mbsf. To achieve this, the model was run to steady-state until a good fit of the POC and sulfate data below 2 mbsf was attained (modeled profiles not shown). This required a POC flux of 2.4×10^{-4} g cm^{-2} yr^{-1} and an initial age, a_0, of 300 kyr (Table 3). For the pre-Holocene setting, the total POC mineralization rate was 1.93 μmol cm^{-2} yr^{-1} (Table 4). Sulfate was consumed via organic matter mineralization at a rate of 0.67 μmol cm^{-2} yr^{-1}, while the AOM rate was 0.18 μmol cm^{-2} yr^{-1}.

Subsequently (Scenario #1), we attempted to fit the measured data in the reference core by increasing the POC flux (F_{POC}) over the last 10 kyr using the following function:

$$F_{POC}(t) = b1 + (b2 \times (\text{Erf}[(t-c1)/c2])) \qquad (19)$$

where $b1$–$b2$ represents the POC flux before the change 10 kyr ago, $2 \times b2$ represents the increase in POC flux during the last 10 kyr, $b1 + b2$ represents the present-day POC flux, $c1$ is half of the perturbation length and $c2$ controls the rate of change of the POC flux. The schematic illustration of function (19) is shown in Fig. 3a. Using the steady-state model results as the initial conditions ($t = 0$ yr), the transient increase in POC content was tuned to the data by adjusting parameters $b1$, $b2$, $c1$ and $c2$ (ensuring that $b1$–$b2 = 2.4 \times 10^{-4}$ g cm^{-2} yr^{-1}) (Table 5). The results (black curves, Fig. 2) show that the POC data could be simulated by increasing the flux from 2.4×10^{-4} to 3.6×10^{-4} g cm^{-2} yr^{-1} over 8 kyr followed by a constant POC flux for the last 2 kyr. However, the resulting model fits to sulfate, DIC and $\delta^{34}S$-SO_4^{2-} were poor, whereby sulfate concentrations were too high in the upper ca. 10 m sediments and DIC and $\delta^{34}S$-SO_4^{2-} were too low (Fig. 2). This indicates that the additional POC arriving at the seafloor during the Holocene was too unreactive in the simulations, implying that it may also have been more labile.

We tested this idea (Scenario #2) by decreasing a_0 as POC flux increased. However, according to Eq. (9), a_0 is a fixed constant, and a

Table 4

Depth-integrated turnover rates and benthic fluxes.[a]

	C9 (before 10 kyr)	C9 (present day)	C14 (present day)	Tai-Nan [b]	Yung-An [b]
F_{POC}: total POC mineralization rate (μmol cm^{-2} yr^{-1} of C)	1.93	11.8	10.1	1.94	10.2
F_{SR}: sulfate reduction via POC degradation (μmol cm^{-2} yr^{-1} of SO$_4^{2-}$)	0.67	5.5	4.5	0.47	3.9
F_M: methane formation via POC degradation (μmol cm^{-2} yr^{-1} of CH$_4$)	0.29	0.43	0.46	0.49	1.3
F_{AOM}: anaerobic oxidation of methane (μmol cm^{-2} yr^{-1} of CH$_4$)	0.18	0.24	1.1	2.4	4.8
F_{Ca}: authigenic carbonate precipitation (μmol cm^{-2} yr^{-1} of Ca)	–	3.9	4.8	–	–
Benthic flux of SO$_4^{2-}$ at sediment–water interface (μmol cm^{-2} yr^{-1} of SO$_4^{2-}$)	0.85	5.8	5.5	2.9	8.7
Benthic flux of CH$_4$ at sediment–water interface (μmol cm^{-2} yr^{-1} of CH$_4$)	-0.003	-0.003	-0.01	-0.07	-0.16
Benthic flux of DIC at sediment–water interface (μmol cm^{-2} yr^{-1} of C)	-1.4	-7.3	-5.5	–	–

[a] Negative fluxes are directed upward from the sediments to the bottom water, and vice versa.
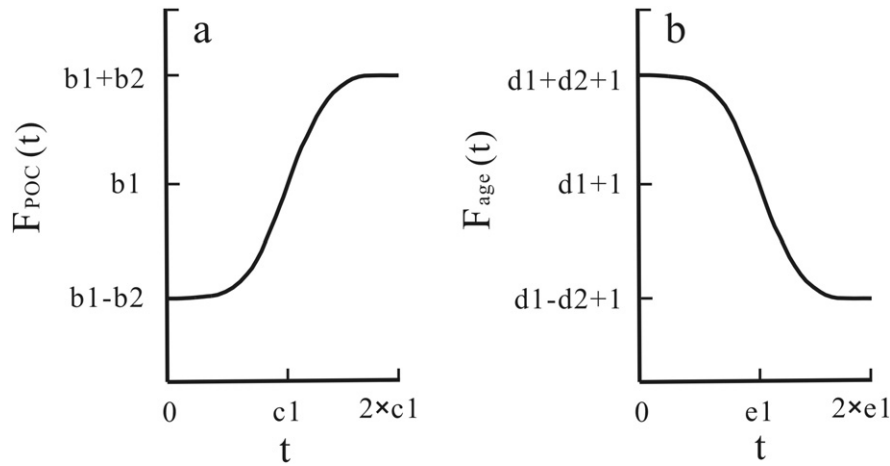[b] Ridges located offshore SW Taiwan, northern SCS (Chuang et al., 2013).

Fig. 3. Schematic plots of the error functions (19) and (20).

decrease in a_0 would affect the whole POC profile simultaneously and not only the new material arriving at the seafloor. We sidestepped this problem by simulating a_0 as a dummy conservative solid variable that is transported through the sediment at the same rate as POC (Eq. (2)). In this case, the upper boundary condition for a_0 was described analogously to Eq. (19):

$$F_{age}(t) = d1 + (1 - d2 \times (Erf[(t - e1)/e2])) \quad (20)$$

where $d1$ and $d2$ determine the maximum and minimum F_{age}, respectively (Fig. 3b), and $e1$ and $e2$ are defined identical to $c1$ and $c2$. In this way, the initial age of POC in each modeled depth layer can be adjusted over time by varying F_{age}. F_{age} was decreased from the previous steady-state model results as POC flux increased (Eq. (19)) for a period of 10 kyr. Parameters $d1$ and $d2$ were tuned to the data as before (Table 5).

Taking this approach, the model is able to simulate the measured POC content as well as sulfate and DIC concentrations (red curves, Fig. 2) by allowing the initial age to decrease from 300 to 0.5 kyr over the last 10 kyr (Fig. 2h). $\delta^{34}S\text{-}SO_4^{2-}$ is also well simulated using a fractionation factor for sulfate reduction of 1.045, which is a typical value for marine sediments (Canfield and Teske, 1996). This represents a significant freshening of the POC arriving at the seafloor from the older, probably reworked, material that characterized the early Holocene. The initial ages used to derive these results are well within the range of values reported for modern continental margin sediments (10^2 to 10^4 yr, Middelburg (1989); Boudreau and Ruddick (1991)). Carbonate precipitation was also required to simulate the DIC concentrations in the last 10 kyr of the non-steady-state model run. Without it, DIC concentrations in the upper 1.5 mbsf are around twice the measured values (data not shown).

Under this present-day condition, total POC mineralization rate (R_{POC}) decreases sharply by two orders-of-magnitude within the upper ca. 2 m compared to the pre-Holocene setting (Fig. 2e). The depth-integrated rate of total POC mineralization is 11.8 μmol cm^{-2} yr^{-1} which is roughly one order-of-magnitude higher than 10 kyr ago (Table 4). The vast majority of sulfate is consumed by OSR at a rate of 5.53 μmol cm^{-2} yr^{-1} while sulfate consumption by AOM is 0.24 μmol cm^{-2} yr^{-1}. The depth-integrated rate of DIC production including OSR and AOM is 11.34 μmol cm^{-2} yr^{-1}. Authigenic carbonate precipitation removes DIC at a rate of 3.92 μmol cm^{-2} yr^{-1} whereas the diffusive flux of DIC to the surface is 7.33 μmol cm^{-2} yr^{-1}. Thus, ca. 35% of total DIC generated in the sediments is removed via authigenic carbonate precipitation.

### 5.2. The minimum age of pockmark formation

Mega-pockmarks are usually formed by intense fluid expulsion and later reshaped by external forcings such as bottom currents (Hovland et al., 2002; Cathles et al., 2010). Long-term observations suggest that pockmarks do not necessarily require persistent fluid venting to maintain their shape (Brothers et al., 2011). A long quiescent or micro-seepage period may follow the expulsion of over-pressured fluid and, hence, most pockmarks in hemipelagic and pelagic sediments are currently dormant (Judd and Hovland, 2007; Paull et al., 2008). After the dormancy prevails, the porewater distribution of solutes will vary over time as the system relaxes toward the new steady-state situation where solute transport is dominated by molecular diffusion. Thus, if the geochemical characteristics of the active seep can be estimated, the time elapsed since the last major seepage event in a dormant seep may be constrained from the present-day porewater distributions by simulating their evolution following the cessation of fluid flow.

We took this approach to estimate the minimum age of pockmark formation in the study area by modeling measured data sampled from an extinct mega-pockmark (C14). The data bear many similarities to the reference core, demonstrated by the inflections in the profiles POC content in the upper 1–2 mbsf as well as for sulfate and $\delta^{34}S\text{-}SO_4^{2-}$ (Fig. 4). This implies that the early Holocene changes inferred from the reference core also apply to the pockmark core. As an initial condition, it is not unreasonable to suggest that the active pockmarks in the study area had a similar biogeochemistry to the well-studied and

Table 5
Derived parameters of the error functions describing the upper boundary conditions for POC and initial age in the reference core (C9) and pockmark core (C14). In Scenario #1, the POC flux was varied for the reference core (C9) only. In Scenario #2, both the POC flux and the initial age were varied in both cores (see text).

|	Parameter	C9	C14	Unit
Scenario #1 (change of POC flux only)	b1	3.0×10^{-4}	–	g cm^{-2} yr^{-1}
	b2	0.6×10^{-4}	–	g cm^{-2} yr^{-1}
	c1	4000	–	yr
	c2	1500	–	yr
Scenario #2 (change of POC flux and initial age)	b1	3.0×10^{-4}	2.6×10^{-4}	g cm^{-2} yr^{-1}
	b2	0.6×10^{-4}	0.6×10^{-4}	g cm^{-2} yr^{-1}
	c1	4000	33000	yr
	c2	1500	1500	yr
	d1	4010	4010	–
	d2	3990	3990	–
	e1	4000	33000	yr
	e2	1500	1500	yr
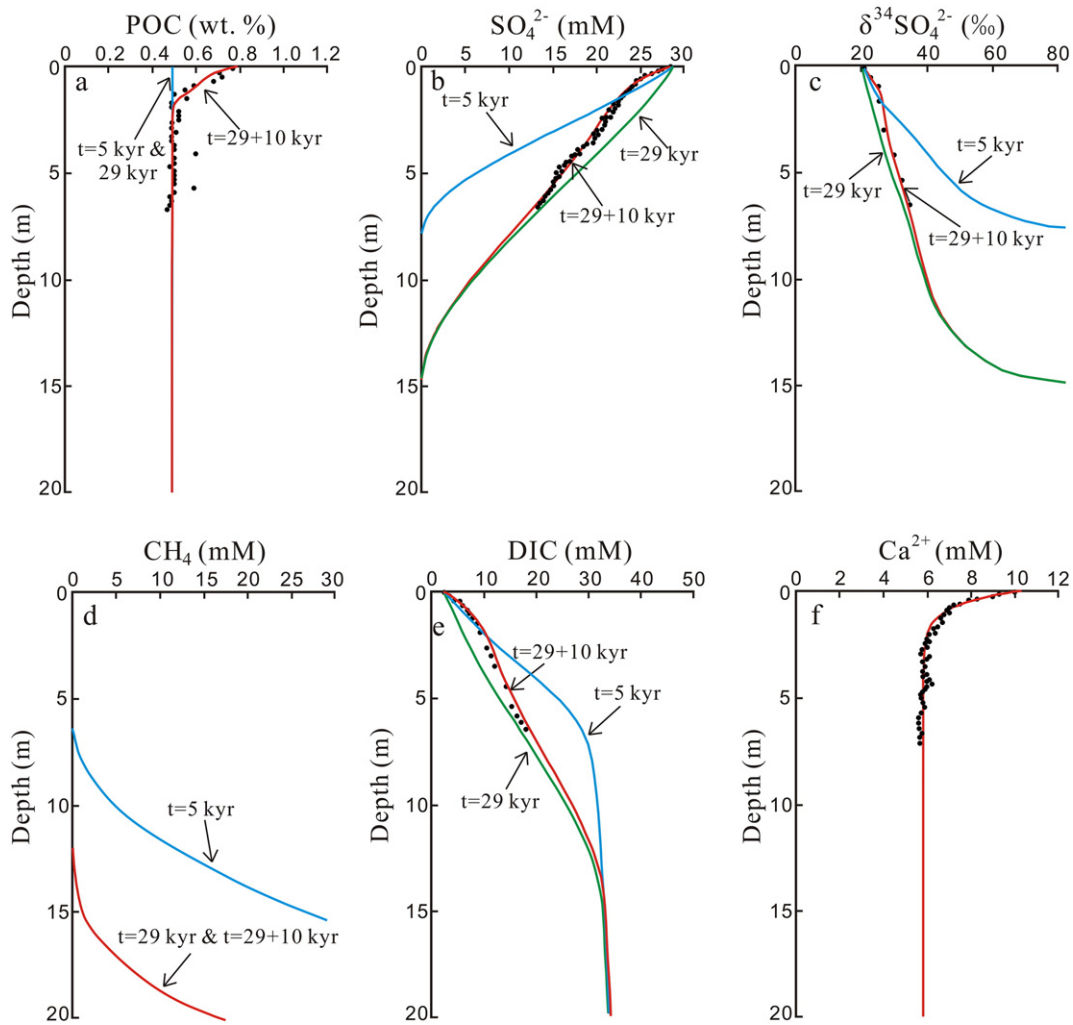
Fig. 4. Transient state model results showing the evolution of (a) POC, (b) sulfate, (c) $\delta^{34}S$-SO_4^{2-}, (d) methane, and (e) DIC in core C14 starting from the initial conditions in Fig. 5. Symbols represent measured data. Profiles are shown for 5, 29, and 29 + 10 kyr. The model results fit the measured values after running for a period of 29 + 10 kyr. The simulated Ca^{2+} concentration profile during the last 10 kyr is shown in (f). Note that only the upper 20 m are shown for each variable.

currently active Hydrate Ridge cold-seep. Both in-situ measurements and modeling results indicated heterogeneous but moderately high fluid flow rates (>10 cm yr^{-1}) (Tryon et al., 2002; Luff and Wallmann, 2003). Sulfate penetrates no deeper than several decimeters below seafloor and methane concentrations are in equilibrium with gas hydrate

(ca. 70 mM) below a thin transition zone where sulfate and methane are consumed by AOM (Torres et al., 2002).

Starting from $t = 0$ yr and using these general profile characteristics as initial conditions (Fig. 5), the model was run forward in time until the present-day data were simulated. During this period, the sulfate
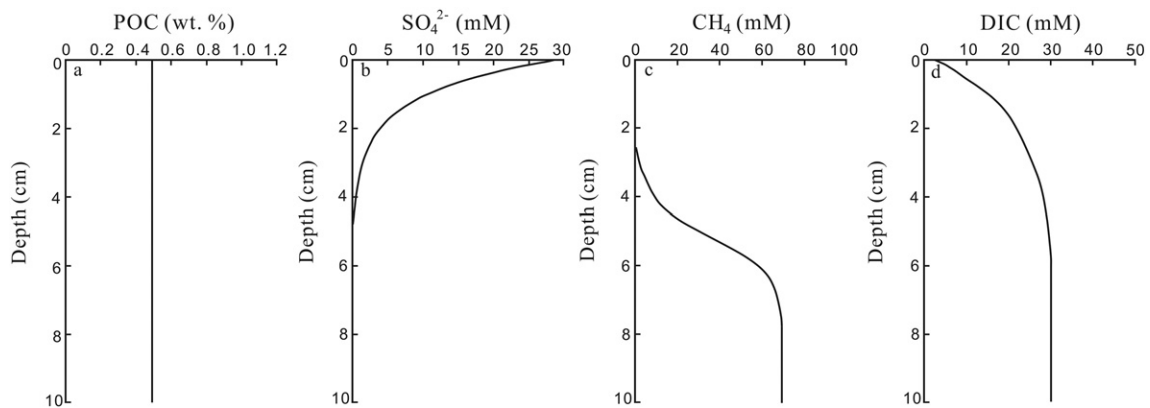
Fig. 5. Hypothetical initial conditions of (a) POC, (b) sulfate, (c) methane, and (d) DIC for an active pockmark seep. POC content was set equal to the measured data below ca. 1 mbsf in core C14 (Fig. 4). Solute concentration profiles are based on observations at Hydrate Ridge (Luff and Wallmann, 2003). Only the upper 10 m are shown. All concentrations are invariable from 10 mbsf down to the base of the simulated sediment column (100 m).
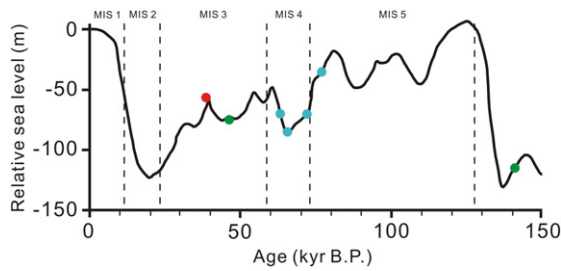
Fig. 6. Global sea level changes during the last 150 kyr for different Marine Isotope Stages, MIS (after Siddall et al. (2003)). The red circle shows the sea level at the proposed time (39 kyr B. P.) when seepage at the pockmark ended. Blue (Tong et al., 2013) and green (Han et al., 2014) circles denote the U/Th dating of authigenic carbonates collected from Dongsha Area, northern SCS.

penetration depth increased over time as the rate of sulfate consumption by AOM decreased due to the cessation of upward advection of methane-rich fluid (Fig. 4). Consequently, $\delta^{34}S\text{-}SO_4^{2-}$ decreased as the porewater became less enriched in $^{34}SO_4^{2-}$ and DIC also decreased due to less production by AOM. The measured profiles of sulfate, DIC and $\delta^{34}S\text{-}SO_4^{2-}$ could be reproduced after running the model for 39 kyr (Fig. 4), which represents the time elapsed since the cessation of the last major fluid expulsion event. This includes the 10 kyr Holocene change in upper boundary conditions. Note that the flux of POC was slightly different from the parameterization for the reference core, which may be due to minor differences in sediment accumulation rate between the two sites (Table 5).

The contemporary total POC mineralization rate in the pockmark core is similar to the reference core and those collected from Yung-An Ridge, offshore SW Taiwan with the POC initial age of 2 kyr (Table 4). Sulfate is removed by OSR at a rate of 4.52 μmol cm^{-2} yr^{-1} and AOM reaches 1.11 μmol cm^{-2} yr^{-1}, which is roughly five times higher than that in C9. The AOM rates in our study area are much lower than those reported for Tai-Nan and Yung-An ridges (Chuang et al., 2013)

because those sites are characterized by upward gas bubble transport and dissolution. DIC is consumed via authigenic carbonate precipitation at 4.84 μmol cm^{-2} yr^{-1} and its flux toward the bottom water is 5.53 μmol cm^{-2} yr^{-1} (Table 4). Near-zero benthic methane flux at both sites suggests that AOM is an effective "microbial filter" that consumes almost all dissolved methane ascending from underlying sediments. Dissolved methane has been demonstrated to only discharge into bottom water at high fluid flow velocities whereas slow seepage of methane bearing fluid (<5 cm yr^{-1}) does not contribute considerably to the overall methane emission (Luff and Wallmann, 2003; Niemann et al., 2006; Wallmann et al., 2006b; Vanneste et al., 2011; Karaca et al., 2014).

Cold seeps in the northern SCS are characterized by several intermittent fluid release events over the last 330 ± 24 kyr B. P. (Tong et al., 2013; Han et al., 2014). U/Th ages of the ^{18}O-enriched authigenic carbonates collected from the northeastern Dongsha Uplift indicate that authigenic carbonate precipitation was linked to gas hydrate dissociation during sea level low-stands (Tong et al., 2013) (Fig. 6). The termination of fluid seepage at the pockmark derived from the non-steady-state modeling (ca. 39 kyr) occurred while eustatic sea level reached a maximum (Fig. 6). One could speculate that the cessation of fluid flow is linked to the depletion of gas hydrate reservoir following the many sea level fluctuations since the late Pleistocene. Further evidence is required to support this possibility. Alternatively, assuming the methane release event at ca. 47 kyr B. P. recorded in the ^{18}O-enriched authigenic carbonates (Han et al., 2014) was also the last fluid seepage event in the pockmark, it is likely that the relative sea level high-stand at ca. 39 kyr B. P. stabilized the gas hydrate because of the increase in hydrostatic pressure.

A conceptual model of the fluid flow in the pockmark field is proposed as follows. At ca. 47 kyr B. P., fluid seepage was driven by gas hydrate dissolution and subsurface overpressure build-up during a relatively low sea level stand (Fig. 7a). Ensuing sea level rise presumably favored the stabilization of gas hydrates and ended active fluid release at ca. 39 kyr B. P. (Fig. 7b). Subsequently, bottom currents promoted the enlargement of the pockmarks (Sun et al., 2011) (Fig. 7c). Our
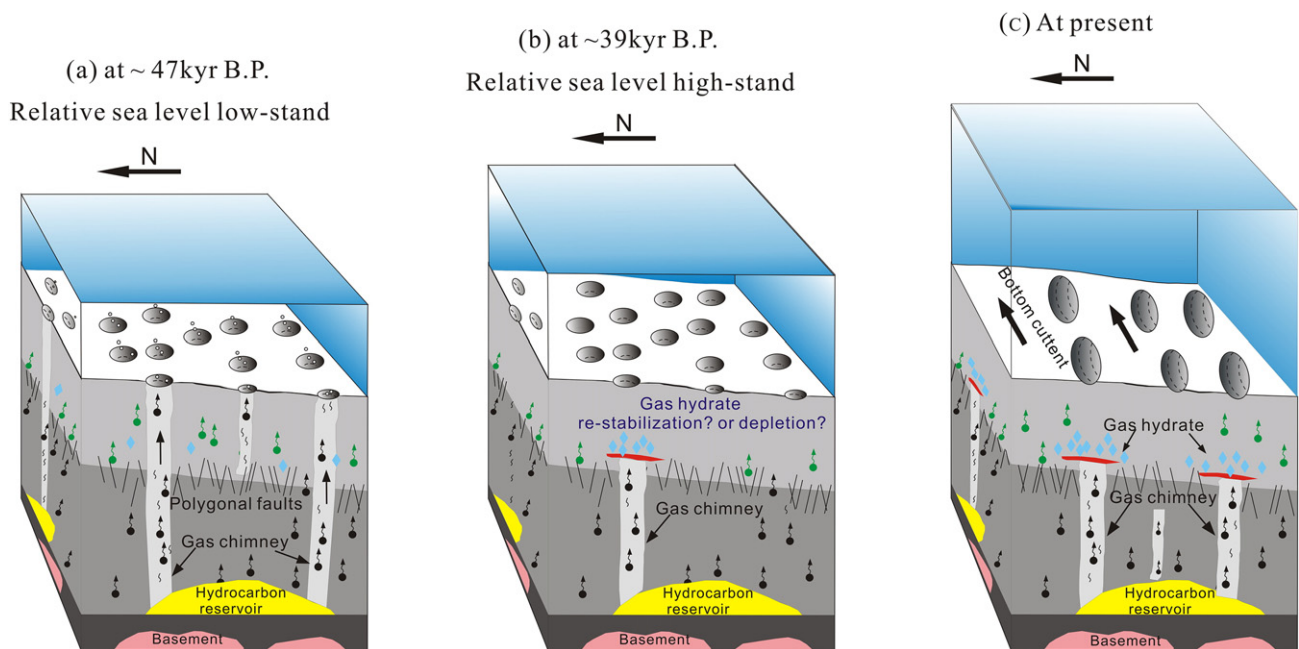
Fig. 7. Proposed schematic representation of the evolutionary history of fluid seepage in the study area. (a) At ca. 47 kyr B. P. fluid seepage occurred due to gas hydrate dissociation during relative sea level low-stand. This age based on authigenic carbonate dating is assumed to be the timing of the last fluid seepage event in the pockmark field. (b) At ca. 39 kyr B. P., fluid seepage ceased owing to either gas hydrate re-stabilization during relative sea level high-stand or the total depletion of gas hydrate reservoir. (c) Recharging of gas hydrate reservoir within the gas hydrate stability zone in the pockmark field during present-day sea level high-stand. Pockmarks have since evolved into mega-pockmarks after being reshaped by bottom currents.

model results are consistent with no fluid seepage from ca. 39 kyr B. P. to the last glacial maximum (LGM, ca 20 kyr B. P.) inferred from the absence of authigenic carbonate spanning this time period (Fig. 6) despite a continual decrease in the sea level. There is evidence that surface sea temperature decreased from ca. 50 kyr B. P. until the LGM and several indications for Heinrich cold events since mid-MIS 3 were recorded in the sediment cores in the northern SCS (Tang et al., 2003; Wei et al., 2007). A decrease in bottom water temperature from ca. 4 °C (Han et al., 2014) at ca. 47 kyr B. P. to ca. − 1.2 °C (Adkins et al., 2002) at the LGM would counteract gas hydrate destabilization induced by a pressure decrease of 6 bar, equivalent to a drop in sea level by 60 m (Siddall et al., 2003). This may explain the absence of fluid seepage between 39 kyr B. P. and the LGM as indicated by the U/Th dating of authigenic carbonate collected from Dongsha, northern SCS (Tong et al., 2013; Han et al., 2014).

6. Conclusions

Porewater geochemical profiles in sediments sampled at a reference core and pockmark core were simulated using a non-steady-state reaction-transport model in order to estimate the time when pockmark activity ceased, which represents the minimum age of the pockmark. The model suggests that the pockmarks formed at least 39 kyr B. P. and the termination of fluid seepage may be ascribed to gas hydrate stabilization or complete depletion when sea level reached a relatively high-stand. We were also able to show that POC flux and reactivity increased during the Holocene due to enhanced primary and export production related to the monsoon. This is, to our knowledge, the first study that uses a reaction-transport model to constrain the cessation of fluid flow at pockmarks. The proposed method could be a significant tool in illuminating temporal evolution of fluid seepage in pockmarks because most pockmarks on continental margins are presently dormant (Judd and Hovland, 2007; Paull et al., 2008), especially if a reliable age-control is lacking.

References

Adkins, J.F., McIntyre, K., Schrag, D.P., 2002. The salinity, temperature, and δ18O of the glacial deep ocean. Science 298, 1769–1773.
Andresen, K.J., Huuse, M., 2011. 'Bulls-eye'pockmarks and polygonal faulting in the Lower Congo Basin: relative timing and implications for fluid expulsion during shallow burial. Mar. Geol. 279, 111–127.
Archer, D.E., Buffett, B.A., 2012. A two-dimensional model of the methane cycle in a sedimentary accretionary wedge. Biogeosciences 9, 2967–3002.
Berndt, C., 2005. Focused fluid flow in passive continental margins. Phil. Trans. R. Soc. A 363, 2855–2871.
Berner, R.A., 1980. Early Diagenesis: A Theoretical Approach. Princeton University Press, Princeton.
Boetius, A., Ravenschlag, K., Schubert, C.J., Rickert, D., Widdel, F., Gieseke, A., Amann, R., Jørgensen, B.B., Witte, U., Pfannkuche, O., 2000. A marine microbial consortium apparently mediating anaerobic oxidation of methane. Nature 407, 623–626.
Borowski, W.S., Paull, C.K., Ussler, W., 1999. Global and local variations of interstitial sulfate gradients in deep-water, continental margin sediments: sensitivity to underlying methane and gas hydrates. Mar. Geol. 159, 131–154.
Boudreau, B.P., 1997. Diagenetic Models and Their Implementation: Modelling Transport and Reactions in Aquatic Sediments. Springer, Berlin.
Boudreau, B.P., Ruddick, B.R., 1991. On a reactive continuum representation of organic matter diagenesis. Am. J. Sci. 291, 507–538.
Bouriak, S., Vanneste, M., Saoutkine, A., 2000. Inferred gas hydrates and clay diapirs near the Storegga Slide on the southern edge of the Vøring Plateau, offshore Norway. Mar. Geol. 163, 125–148.
Brothers, L.L., Kelley, J.T., Belknap, D.F., Barnhardt, W.A., Andrews, B.D., Maynard, M.L., 2011. More than a century of bathymetric observations and present-day shallow sediment characterization in Belfast Bay, Maine, USA: implications for pockmark field longevity. Geo-Mar. Lett. 31, 237–248.
Canfield, D.E., Teske, A., 1996. Late Proterozoic rise in atmospheric oxygen concentration inferred from phylogenetic and sulphur-isotope studies. Nature 382, 127–132.
Cathles, L., Su, Z., Chen, D., 2010. The physics of gas chimney and pockmark formation, with implications for assessment of seafloor hazards and gas sequestration. Mar. Pet. Geol. 27, 82–91.
Chen, J., Li, H., Jin, H., Chen, F., Wiesner, M., Zheng, L., 2010. A preliminary discussion and evaluation of paleo-production proxies in the South China Sea. J. Mar. Sci. 28, 1–10 (in Chinese with English abstract).
Chernyavsky, B.M., Wortmann, U.G., 2007. REMAP: a reaction transport model for isotope ratio calculations in porous media. Geochem. Geophys. Geosyst. 8, Q02009. http://dx.doi.org/10.1029/02006GC001442.
Chow, J., Lee, J.S., Sun, R., Liu, C.S., Lundberg, N., 2000. Characteristics of the bottom simulating reflectors near mud diapirs: offshore southwestern Taiwan. Geo-Mar. Lett. 20, 3–9.
Chuang, P.-C., Dale, A.W., Wallmann, K., Haeckel, M., Yang, T.F., Chen, N.-C., Chen, H.-C., Chen, H.-W., Lin, S., Sun, C.-H., You, C.-F., Horng, C.-S., Wang, Y., Chung, S.-H., 2013. Relating sulfate and methane dynamics to geology: accretionary prism offshore SW Taiwan. Geochem. Geophys. Geosyst. 14, 2523–2545.
Çifçi, G., Dondurur, D., Ergün, M., 2003. Deep and shallow structures of large pockmarks in the Turkish shelf, Eastern Black Sea. Geo-Mar. Lett. 23, 311–322.
Clift, P., Lin, J., Barckhausen, U., 2002. Evidence of low flexural rigidity and low viscosity lower continental crust during continental break-up in the South China Sea. Mar. Pet. Geol. 19, 951–970.
Cole, D., Stewart, S., Cartwright, J., 2000. Giant irregular pockmark craters in the Palaeogene of the outer Moray Firth basin, UK North Sea. Mar. Pet. Geol. 17, 563–577.
Dale, A.W., Brüchert, V., Alperin, M., Regnier, P., 2009. An integrated sulfur isotope model for Namibian shelf sediments. Geochim. Cosmochim. Acta 73, 1924–1944.
Dickens, G.R., Castillo, M.M., Walker, J.C., 1997. A blast of gas in the latest Paleocene: simulating first-order effects of massive dissociation of oceanic methane hydrate. Geology 25, 259–262.
Feng, D., Roberts, H.H., Cheng, H., Peckmann, J., Bohrmann, G., Lawrence Edwards, R., Chen, D., 2010. U/Th dating of cold-seep carbonates: an initial comparison. Deep-Sea Res. II Top. Stud. Oceanogr. 57, 2055–2060.
Foucher, J.P., Westbrook, G., Boetius, A., Ceramicola, S., Dupré, S., Mascle, J., Mienert, J., Pfannkuche, O., Pierre, C., Praeg, D., 2009. Structure and drivers of cold seep ecosystems. Oceanography 22, 92–109.
Froelich, P.N., Klinkhammer, G.P., Bender, M.L., Luedtke, N.A., Heath, G.R., Cullen, D., Dauphin, P., Hammond, D., Hartman, B., Maynard, V., 1979. Early oxidation of organic matter in pelagic sediments of the eastern equatorial Atlantic: suboxic diagenesis. Geochim. Cosmochim. Acta 43, 1075–1090.
Habicht, K.S., Canfield, D.E., 1997. Sulfur isotope fractionation during bacterial sulfate reduction in organic-rich sediments. Geochim. Cosmochim. Acta 61, 5351–5361.
Han, X., Suess, E., Liebetrau, V., Eisenhauer, A., Huang, Y., 2014. Past methane release events and environmental conditions at the upper continental slope of the South China Sea: constraints by seep carbonates. Int. J. Earth Sci. 103, 1873–1887.
Hartwig, A., Anka, Z., di Primio, R., 2012. Evidence of a widespread paleo-pockmarked field in the Orange Basin: an indication of an early Eocene massive fluid escape event offshore South Africa. Mar. Geol. 332–334, 222–234.
He, Z., Liu, Z., Li, J., Xie, X., 2012. Elemental geochemical records in the western South China Sea since 540 ka and their paleoenvironmental implications. Adv. Earth Sci. 27, 327–336 (in Chinese with English abstract).
Heggland, R., 1998. Gas seepage as an indicator of deeper prospective reservoirs. A study based on exploration 3D seismic data. Mar. Pet. Geol. 15, 1–9.
Hensen, C., Zabel, M., Pfeifer, K., Schwenk, T., Kasten, S., Riedinger, N., Schulz, H.D., Boetius, A., 2003. Control of sulfate pore-water profiles by sedimentary events and the significance of anaerobic oxidation of methane for the burial of sulfur in marine sediments. Geochim. Cosmochim. Acta 67, 2631–2647.
Hill, T., Paull, C., Critser, R., 2012. Glacial and deglacial seafloor methane emissions from pockmarks on the northern flank of the Storegga Slide complex. Geo-Mar. Lett. 32, 73–84.
Hovland, M., Svensen, H., 2006. Submarine pingoes: indicators of shallow gas hydrates in a pockmark at Nyegga, Norwegian Sea. Mar. Geol. 228, 15–23.
Hovland, M., Gardner, J., Judd, A., 2002. The significance of pockmarks to understanding fluid flow processes and geohazards. Geofluids 2, 127–136.
Hovland, M., Svensen, H., Forsberg, C.F., Johansen, H., Fichler, C., Fosså, J.H., Jonsson, R., Rueslåtten, H., 2005. Complex pockmarks with carbonate-ridges off mid-Norway: products of sediment degassing. Mar. Geol. 218, 191–206.
Huang, B.J., Xiao, X.M., Li, X.X., 2003. Geochemistry and origins of natural gases in the Yinggehai and Qiongdongnan basins, offshore South China Sea. Org. Geochem. 34, 1009–1025.
Hustoft, S., Bünz, S., Mienert, J., Chand, S., 2009a. Gas hydrate reservoir and active methane-venting province in sediments on <20 Ma young oceanic crust in the Fram Strait, offshore NW-Svalbard. Earth Planet. Sci. Lett. 284, 12–24.
Hustoft, S., Dugan, B., Mienert, J., 2009b. Effects of rapid sedimentation on developing the Nyegga pockmark field: constraints from hydrological modeling and 3-D seismic data, offshore mid-Norway. Geochem. Geophys. Geosyst. 10, 1–17.
Jørgensen, B.B., 1979. A theoretical model of the stable sulfur isotope distribution in marine sediments. Geochim. Cosmochim. Acta 43, 363–374.

Jørgensen, B.B., Kasten, S., 2006. Sulfur cycling and methane oxidation. In: Schulz, H.D., Zabel, M. (Eds.), Marine Geochemistry, 2nd ed. Springer, Berlin, pp. 271–309.

Judd, A.G., Hovland, M., 2007. Seabed Fluid Flow: The Impact of Geology, Biology and the Marine Environment. Cambridge Univ Pr.

Judd, A.G., Hovland, M., Dimitrov, L., Garcia Gil, S., Jukes, V., 2002. The geological methane budget at continental margins and its influence on climate change. Geofluids 2, 109–126.

Karaca, D., Schleicher, T., Hensen, C., Linke, P., Wallmann, K., 2014. Quantification of methane emission from bacterial mat sites at Quepos Slide offshore Costa Rica. Int. J. Earth Sci. 103, 1817–1829.

León, R., Somoza, L., Medialdea, T., Hernández-Molina, F.J., Vázquez, J.T., Díaz-del-Rio, V., González, F.J., 2010. Pockmarks, collapses and blind valleys in the Gulf of Cádiz. Geo-Mar. Lett. 30, 231–247.

Liu, K.-K., Chao, S.-Y., Shaw, P.-T., Gong, G.-C., Chen, C.-C., Tang, T., 2002. Monsoon-forced chlorophyll distribution and primary production in the South China Sea: observations and a numerical study. Deep-Sea Res. I Oceanogr. Res. Pap. 49, 1387–1412.

Lüdmann, T., Wong, H.K., Berglar, K., 2005. Upward flow of North Pacific Deep Water in the northern South China Sea as deduced from the occurrence of drift sediments. Geophys. Res. Lett. 32, L05614.

Luff, R., Wallmann, K., 2003. Fluid flow, methane fluxes, carbonate precipitation and biogeochemical turnover in gas hydrate-bearing sediments at Hydrate Ridge, Cascadia Margin: numerical modeling and mass balances. Geochim. Cosmochim. Acta 67, 3403–3421.

Luo, M., Chen, L., Wang, S., Yan, W., Wang, H., Chen, D., 2013. Pockmark activity inferred from pore water geochemistry in shallow sediments of the pockmark field in southwestern Xisha Uplift, northwestern South China Sea. Mar. Pet. Geol. 48, 247–259.

Luo, M., Chen, L., Tong, H., Yan, W., Chen, D., 2014. Gas hydrate occurrence inferred from dissolved Cl⁻ concentrations and δ¹⁸O values of pore water and dissolved sulfate in the shallow sediments of the pockmark field in southwestern Xisha Uplift, northern South China Sea. Energies 7, 3886–3899.

MacDonald, I., Leifer, I., Sassen, R., Stine, P., Mitchell, R., Guinasso, N., 2002. Transfer of hydrocarbons from natural seeps to the water column and atmosphere. Geofluids 2, 95–107.

Middelburg, J.J., 1989. A simple rate model for organic matter decomposition in marine sediments. Geochim. Cosmochim. Acta 53, 1577–1581.

Minshull, T., White, R., 1989. Sediment compaction and fluid migration in the Makran accretionary prism. J. Geophys. Res. Solid Earth 94, 7387–7402.

Mogollón, J., Dale, A.W., Fossing, H., Regnier, P., 2012. Timescales for the development of methanogenesis and free gas layers in recently-deposited sediments of Arkona Basin (Baltic Sea). Biogeosciences 9, 1915–1933.

Moss, J., Cartwright, J., Cartwright, A., Moore, R., 2012. The spatial pattern and drainage cell characteristics of a pockmark field, Nile Deep Sea Fan. Mar. Pet. Geol. 35, 321–336.

Niemann, H., Duarte, J., Hensen, C., Omoregie, E., Magalhaes, V., Elvert, M., Pinheiro, L., Kopf, A., Boetius, A., 2006. Microbial methane turnover at mud volcanoes of the Gulf of Cadiz. Geochim. Cosmochim. Acta 70, 5336–5355.

Oelkers, E.H., Helgeson, H.C., 1991. Calculation of activity coefficients and degrees of formation of neutral ion pairs in supercritical electrolyte solutions. Geochim. Cosmochim. Acta 55, 1235–1251.

Paull, C., Ussler Iii, W., Maher, N., Greene, H., Rehder, G., Lorenson, T., Lee, H., 2002. Pockmarks off Big Sur, California. Mar. Geol. 181, 323–335.

Paull, C.K., Ussler III, W., Holbrook, W.S., Hill, T.M., Keaten, R., Mienert, J., Haflidason, H., Johnson, J.E., Winters, W.J., Lorenson, T.D., 2008. Origin of pockmarks and chimney structures on the flanks of the Storegga Slide, offshore Norway. Geo-Mar. Lett. 28, 43–51.

Pilcher, R., Argent, J., 2007. Mega-pockmarks and linear pockmark trains on the West African continental margin. Mar. Geol. 244, 15–32.

Reeburgh, W.S., 1976. Methane consumption in Cariaco Trench waters and sediments. Earth Planet. Sci. Lett. 28, 337–344.

Regnier, P., Dale, A.W., Arndt, S., LaRowe, D., Mogollón, J., Van Cappellen, P., 2011. Quantitative analysis of anaerobic oxidation of methane (AOM) in marine sediments: a modeling perspective. Earth Sci. Rev. 106, 105–130.

Robison, C., Elrod, L., Bissada, K., 1998. Petroleum generation, migration, and entrapment in the Zhu 1 depression, Pearl River Mouth basin, South China Sea. Int. J. Coal Geol. 37, 155–178.

Siddall, M., Rohling, E.J., Almogi-Labin, A., Hemleben, C., Meischner, D., Schmelzer, I., Smeed, D.A., 2003. Sea-level fluctuations during the last glacial cycle. Nature 423, 853–858.

Su, X., Liu, C., Li, J., 2007. Coccolith evidence for variations in upper ocean water in upwelling area off the coast of Vietnam for the past 450,000 years. Mar. Geol. Quat. Geol. 27, 71–76 (in Chinese with English abstract).

Suess, E., Torres, M., Bohrmann, G., Collier, R., Greinert, J., Linke, P., Rehder, G., Trehu, A., Wallmann, K., Winckler, G., 1999. Gas hydrate destabilization: enhanced dewatering, benthic material turnover and large methane plumes at the Cascadia convergent margin. Earth Planet. Sci. Lett. 170, 1–15.

Sun, Q., Wu, S., Hovland, M., Luo, P., Lu, Y., Qu, T., 2011. The morphologies and genesis of mega-pockmarks near the Xisha Uplift, South China Sea. Mar. Pet. Geol. 28, 1146–1156.

Sun, Q., Wu, S., Cartwright, J., Lüdmann, T., Yao, G., 2012a. Focused fluid flow systems of the Zhongjiannan Basin and Guangle Uplift, South China Sea. Basin Res. 2, 1–15.

Sun, Y., Wu, S., Dong, D., Lüdmann, T., Gong, Y., 2012b. Gas hydrates associated with gas chimneys in fine-grained sediments of the northern South China Sea. Mar. Geol. 311, 32–40.

Sun, Q., Cartwright, J., Wu, S., Chen, D., 2013. 3D Seismic Interpretation of Dissolution Pipes in the South China Sea: Genesis by Subsurface, Fluid Induced Collapse. Marine Geology.

Tang, X., Chen, Z., Yan, W., Chen, M., 2003. Youger Dryas and Heinrich events recorded by magnetic susceptibility of sediments from the central temperature area of Western Pacific Warm Pool. Chin. Sci. Bull. 48, 808–813.

Taviani, M., Angeletti, L., Ceregato, A., Foglini, F., Froglia, C., Trincardi, F., 2013. The Gela Basin pockmark field in the strait of Sicily (Mediterranean Sea): chemosymbiotic faunal and carbonate signatures of postglacial to modern cold seepage. Biogeosciences 10, 967–1009.

Tian, Z., Long, A., Chen, S., 2004. Review of paleoproductivity research in South China Sea. Mar. Sci. 28, 65–71 (in Chinese).

Tong, H., Feng, D., Cheng, H., Yang, S., Wang, H., Min, A.G., Lawrence Edwards, R., Chen, Z., Chen, D., 2013. Authigenic carbonates from seeps on the northern continental slope of the South China Sea: new insights into fluid sources and geochronology. Mar. Pet. Geol. 43.

Torres, M., McManus, J., Hammond, D., De Angelis, M., Heeschen, K., Colbert, S., Tryon, M., Brown, K., Suess, E., 2002. Fluid and chemical fluxes in and out of sediments hosting methane hydrate deposits on Hydrate Ridge, OR, I: hydrological provinces. Earth Planet. Sci. Lett. 201, 525–540.

Tryon, M., Brown, K., Torres, M., 2002. Fluid and chemical flux in and out of sediments hosting methane hydrate deposits on Hydrate Ridge, OR, II: hydrological processes. Earth Planet. Sci. Lett. 201, 541–557.

Van Cappellen, P., Wang, Y., 1996. Cycling of iron and manganese in surface sediments; a general theory for the coupled transport and reaction of carbon, oxygen, nitrogen, sulfur, iron, and manganese. Am. J. Sci. 296, 197–243.

Vanneste, H., Kelly-Gerreyn, B.A., Connelly, D.P., James, R.H., Haeckel, M., Fisher, R.E., Heeschen, K., Mills, R.A., 2011. Spatial variation in fluid flow and geochemical fluxes across the sediment–seawater interface at the Carlos Ribeiro mud volcano (Gulf of Cadiz). Geochim. Cosmochim. Acta 75, 1124–1144.

Wallmann, K., Aloisi, G., Haeckel, M., Obzhirov, A., Pavlova, G., Tishchenko, P., 2006a. Kinetics of organic matter degradation, microbial methane generation, and gas hydrate formation in anoxic marine sediments. Geochim. Cosmochim. Acta 70, 3905–3927.

Wallmann, K., Drews, M., Aloisi, G., Bohrmann, G., 2006b. Methane discharge into the Black Sea and the global ocean via fluid flow through submarine mud volcanoes. Earth Planet. Sci. Lett. 248, 545–560.

Wang, P., Prell, W., Blum, P., 2000. Proceeding of the Ocean Drilling Program: Initial Reports 184. Texas A&M University, College Station, TX, USA.

Wang, X., Wu, S., Yuan, S., Wang, D., Ma, Y., Yao, G., Gong, Y., Zhang, G., 2010. Geophysical signatures associated with fluid flow and gas hydrate occurrence in a tectonically quiescent sequence, Qiongdongnan Basin, South China Sea. Geofluids 10, 351–368.

Wei, G., Deng, W., Liu, Y., Li, X., 2007. High-resolution sea surface temperature records derived from foraminiferal Mg/Ca ratios during the last 260 ka in the northern South China Sea. Palaeogeogr. Palaeoclimatol. Palaeoecol. 250, 126–138.

Wortmann, U.G., Chernyavsky, B.M., 2011. The significance of isotope specific diffusion coefficients for reaction-transport models of sulfate reduction in marine sediments. Geochim. Cosmochim. Acta 75, 3046–3056.

Xie, X., Muller, R.D., Li, S., Gong, Z., Steinberger, B., 2006. Origin of anomalous subsidence along the Northern South China Sea margin and its relationship to dynamic topography. Mar. Pet. Geol. 23, 745–765.

Zachos, J.C., Dickens, G.R., Zeebe, R.E., 2008. An early Cenozoic perspective on greenhouse warming and carbon-cycle dynamics. Nature 451, 279–283.

Zhu, W., Huang, B., Mi, L., Wilkins, R.W.T., Fu, N., Xiao, X., 2009. Geochemistry, origin, and deep-water exploration potential of natural gases in the Pearl River Mouth and Qiongdongnan basins, South China Sea. AAPG Bull. 93, 741–761.